Investigation of hierarchical structure formation in merocyanine photovoltaics

Tucker L. Murrey,† Dirk Hertel,‡ Julian Nowak,‡ Ruth Bruker,‡ Thorsten Limböck,‡ Jörg Neudörfl,‡ Stephanie Rüth,‡ Jürgen Schelter,‡ Selina Olthof,‡ Aurel Radulescu,¶ Adam J. Moulé,*,§ and Klaus Meerholz‖

†*Department of Material Science and Engineering, University of California, Davis, USA*

‡*Department für Chemie, Universität zu Köln, Greinstraße 4-6, 50939 Köln*

¶*Jülich Centre for Neutron Science, Heinz Maier-Leibnitz Zentrum, Forschungszentrum Jülich GmbH, Lichtenbergstraße 1, 85748 Garching, Germany*

§*Department of Chemical Engineering, University of California, Davis, USA*

‖*Department für Chemie, Universität zu Köln, Luxemburger Straße 116, 50939 Köln*

E-mail: amoule@ucdavis.edu

Abstract

Merocyanines (MC) are a versatile class of small molecule dyes. Their optoelectronic properties are easily tunable by chemically controlling their donor-acceptor strength, and their structural properties can be tuned by simple side chain substitution. This manuscript demonstrates a novel series of MC featuring an indoline donor with varying hydrocarbon side chain length (from 6 to 12 carbons) and a tert-butyl-thiazole acceptor, labeled I*n*TBT. Bulk heterojunction organic photovoltaics are fabricated with a PCBM acceptor and characterized. Films composed of I8TBT:PCBM and I9TBT:PCBM produced the the highest power conversion efficiency of 4.5%, which suggests that the morphology is optimized by controlling the side chain length. Hierarchical structure formation in InTBT:PCBM films are studied using grazing incidence x-ray diffraction (GIXRD), small angle neutron scattering (SANS), and atomic force microscopy (AFM). When mixed with PCBM, InTBTs with ≤ 8 side chain carbons form pure crystalline domains, while InTBTs with ≥ 9 side chain carbons mix well with PCBM. SANS demonstrates that increasing side chain length increases InTBT rich domain size. In addition, a branched hexyl-dodecyl side chain IHDTBT:PCBM film was studied and found to exhibit the worst performance OPV device. The large branched side chain inhibited mixing between IHDTBT and PCBM resulting in large segregated phases.

1 Introduction

An increasing number of donor candidate molecules for organic photovoltaics (OPV) with alternating electron donor (D) and acceptor (A) subunits have been reported in recent years.[1–4] Among simple dyes, dipolar merocyanines (MCs) are an interesting and versatile class of functional materials.[5,6] MC donor-acceptor (D-A) groups can be easily changed to tune their absorption from the blue to IR spectral region, with ground state dipole moments ranging from 3 to 15 D. MCs have been applied as active component in bulk heterojunction (BHJ) OPV devices.[7–10] A previous study by Kronenberg et al. showed that BHJ OPVs composed of indoline based MCs donors and [6,6]-phenyl-C_{61}-butyric acid methyl ester (PCBM) or C_{60} acceptors manifest large open circuit voltages (V_{OC}) and short circuit currents (J_{SC}) of 0.9, 0.76 V and 5.3 , 6.3 $\frac{mA}{cm^2}$ respectively. However poor charge transport gave rise to low fill factors (FF) ($\sim$30%) resulting in power conversion efficiencies (PCE) of 1.5 and 1.7%.[11] Subsequently, Steinmann et al. created a tandem OPV using the same materials resulting in an very high V_{OC} of 2.1 V and PCE of 4.8%, but retained a low FF.[12] So far the highest PCE reported from an indoline based D-A device with a simple BHJ architecture is 6.1% (FF 47%) from a vacuum deposited MC:PCBM device, while the record for solution processed device is 4.5%.[13,14] Both of those devices benefited from improved FFs of 47% and 44% respectively.

Morphology control is currently a major limitation for D-A OPVs. A variety of structural motifs have been obtained for several D-A subunits with varying dipole strength, including but not limited to, simple isolated anti-parallel dimers, stacked dimers (1D), and slipped/staircase like structures.[14,15] Due to the complexity of interactions between neighboring molecules (i.e.: competing sterical interactions, intermolecular van der Waals/dipolar forces, and substrate interactions) there is currently no set of guidelines capable of predicting the solid-state packing from molecular structure. Recently, many new small molecule architectures have been developed to prevent D-A dipole alignment and improve π-π stacking including donor-acceptor-donor (D-A-D), and acceptor-donor-acceptor (A-D-A).[16] The current BHJ OPV record for a small molecule device is held by an A-D-A donor molecule with π-conjugated bridges between the groups denoted as A-π-D-π-A, with a PCE of 14.3%.[17] The cost of synthesizing A-π-D-π-A molecules is considerably larger than for simple D-A compounds. Research into improving BHJ morphology with simple D-A donors is necessary.

Optimizing the structural properties of D-A BHJ OPVs is challenging. To enable efficient charge separation and collection, p-type MC donors must be mixed with an n-type acceptor (i.e. PCBM). The mixture of MC:PCBM in solid state can create a multiphase system with pure MC, pure PCBM, and mixed domains. Domain size, crystal structure, and domain purity must be optimized to promote efficient exciton dissociation, charge transport, and extraction.[18]

In this article, we report a comprehensive investigation of a series of structurally related D-A MC dyes, with varying hydrocarbon side chain length (Figure 1). The choice of MC is based on previous studies which obtained best results, in terms of PV performance, with indoline based donor groups.[2,3] The thiazol-di-cyanovinylene acceptor group was chosen because its high acceptor strength enables H/J type coupling,[19] shows high mobility in crystalline OFETs, and yields a high V_{OC} with PCBM due to favorable ionization energy.[3]

By tuning side chain length we are able to control solubility, molecular packing, and phase segregation in MC:PCBM BHJ OPV devices. The BHJ films are characterized in OPV devices to obtain J-V curves and structural information is obtained using grazing incidence x-ray diffraction (GIXRD), small-angle neutron scattering (SANS), and atomic force microscopy (AFM). Similar to previous studies[20–22] we show that by tuning hydrocarbon side chain length we can control hierarchical structure formation to improve charge extraction in MC based OPVs.

2 Experimental

2.1 Sample Processing:

All OPVs were fabricated on indium-tin oxide (ITO, 125 nm) coated glass. The substrates were exposed to ozone for 3 min and transferred to the evaporation chamber to evaporate 10 nm MoO_3. Substrates were transfered into a glove box to spin coat 70 nm thick active layers from chloroform solutions of 13 to 15 mg/mL mixed in a ratio of 2:3 (InTBT to $PC_{61}BM$). The device fabrication was completed by thermal evaporation of 5 nm Ca then 100 nm Ag.

2.2 UV-Vis:

Absorption measurements were performed using a Lambda 1050 (Perkin Elmer) UV/vis spectrometer. A molar concentration of 10^{-4}-10^{-6} mol/L were used for performing optical absorption measurements in solution.

2.3 Single Crystal XRD:

Measurement of single crystals was done using a Bruker D8 Venture (with software APEX3) in kappa geometry equipped with a copper microfocus source and a Photon100 detector. SADABS[23] was used for analysis, scaling and absorption correction. SHELXT and

SHELXL[24] were used for InTBT structure refinement.

2.4 GIXRD:

GIXRD was collected using a Panalytical Empyrean system with a Cu Kα anode λ=1.54056 Å^{-1}. Glass was used as amorphous substrate. The incidence angle was optimized for every measurement to reduce scattering from substrate and air interfaces. Initially a survey was conducted from θ ~5 to 15° with $\omega = 0.2°$. The most intense $\theta \sim$ peak was used to find the optimal ω for signal and background measurement.[25]

2.5 SANS:

The SANS experiments were completed on KWS-2 SANS instrument at the Heinz Maier-Leibnitz Zentrum (MLZ), Garching, Germany. Three instrument conditions were used to provide Q-values ranging from 0.16 to 0.003 Å^{-1}, where $Q = \frac{4\pi}{\lambda}\sin(\frac{\theta}{2})$; λ is the neutron wavelength and θ is the scattering angle. The first two conditions were collected with a collimation length of 4 m with neutron wavelength 4.66 Å and a sample-detector distances of 1.61m and 3.61 m. For the third condition, the collimation length was 20 m with neutron wavelength 5 Å and sample-detector distance at 19.51 m.

2.6 AFM:

The AFM measurements were performed on a MFP-3d Infinity from Asylum Research. All measurements were conducted in amplitude-modulated alternating contact mode utilizing micro cantilevers of the type OMCL-AC200TS from Olympus Micro Cantilevers. All measurements were conducted under ambient conditions in air.

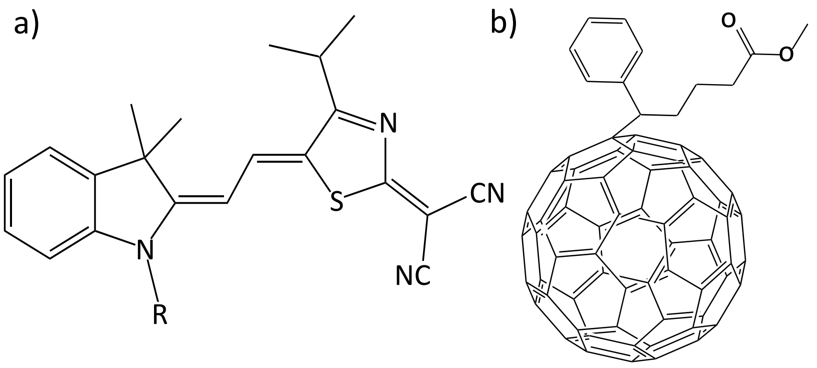

Figure 1: Chemical structures of compounds used in this study: a) a series of MC featuring an indoline donor with varying hydrocarbon side chain length (R) and a tert-butyl-thiazole acceptor, labeled I*n*TBT. b) $PC_{61}BM$.

3 Results

The procedures to synthesize the MC donors can be found in the Supporting Information. We synthesized a series of MCs with varied side chain length on the indolene from hexyl to dodecyl and a derivative with a branched hexyl-dodecyl chain. For the ease of labeling we number the MCs according to the side chain length, i.e. I*n*TBT, with I6TBT for the hexyl side chain and so on to I12TBT and IHDTBT for the branched derivative See Figure 1. The I*n*TBTs with $n > 6$ have a much higher FF ($FF > 0.6$) compared to typical MC cells processed from solution/or vacuum of comparable thickness (Figure 3 a)).[26]

The side chain affects both the solubility and crystal packing but does not change the optical or electronic properties of the dye itself. All I*n*TBT samples have nearly identical UV-vis absorbance at the same molar concentration and solvent quality in solution. The absorption spectra of I8TBT in solutions with varying polarity are shown in Figure S5. The data shows a clear progression from a blue-shifted spectrum in hexane to red-shifted J-aggregates in more polar solvents. Since the I*n*TBT's are less soluble in nonpolar solvents, this progression also shows that a red-shifted UV-vis spectrum with increased 0-0 to 0-1 peak ratio indicates the presence of ordered crystalline aggregates in the film.[10,19] Figure 2 shows UV-vis absorption spectra of all 2:3 wt.% I*n*TBT:PCBM films normalized to the central peak at 590 nm. In these aggregates the coupling between nearest neighbors is strongly

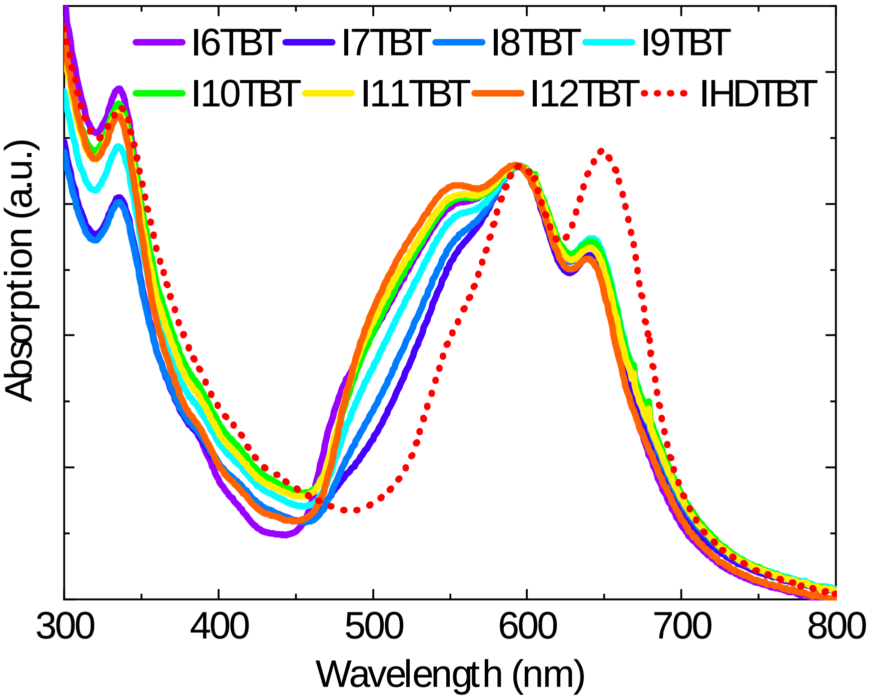

Figure 2: UV-vis absorption spectra of InTBT:PCBM films normalized to the common peak at 594 nm.

influenced by the side chain length.

A clear side chain length trend can be observed in the UV-vis data. The OPV films all share three MC vibronic peaks at ∼650 nm (0-0), ∼600 nm (0-1), and ∼550 nm (0-2) as well as a PCBM peak at ∼350 nm. The linear side chain samples also share an amorphous absorption at ∼500 nm. The spectra are normalized to the central peak of the MC, which allows us to probe the symmetry of the D-A aggregations to be more H-like or J-like and provides information on delocalization. The ratio of the 0-0 to 0-1 transitions ($\frac{0-0}{0-1}$) is fairly constant for all the InTBTs with linear side chains, meaning the aggregations are similar in orientation. As the linear side chain increases in length the 0-2 peak and amorphous absorption increase, indicating that the InTBTs with longer side chains experience additional geometries. The 0-0 and 0-1 transition ratio in the IHDTBT:PCBM film depicts a J-like configuration indicating minimal mixing with PCBM.

We fabricated BHJ OPV devices from solution with InTBT:PCBM in a composition ratio of 2:3 by weight, which means the molar ratio changes as a function of side chain length.[27]

The active layer thickness was kept at a constant 70 nm for all the devices due to the limited solubility of the short and very long side-chain derivatives. The hole collection layer is 10 nm MoO_3 evaporated onto ITO[3] and the anode is composed of 5 nm Ca/100 nm Ag. All of the device fabrication details are in the experimental section. Typical AM1.5 solar simulator JV curves are shown in Figure 3 (a) for all MCs. The JV characteristics are listed in Table 1 and PCE as a function of side chain length is shown in Figure 3 b).

As I*n*TBT side chain length is increased from 6 to 12 carbons, the V_{OC} increases to a maximum at 0.90 ± 0.01 V for I9TBT, I10TBT, and I11TBT before decreasing again. The I6TBT device has the highest short circuit current density (J_{sc}) at 8.29 ± 0.38 $\frac{mA}{cm^2}$ because it has the highest absorbance integral (shortest side chain) seen in the unnormalized UV-vis Figure S6. I11TBT has the highest FF at 0.67 ± 0.01, indicating the most favorable balance of hole and electron transport.[28,29] The highest PCE of 4.5 ± 0.1% was extracted from devices with I8TBT and I9TBT. These films exhibited the best combination of J_{sc} and FF, balancing increased optical absorbance for short side chains and favorable morphology for longer chains. Higher PCE devices could be obtained by optimizing layer thickness and the mixing ratio for I8TBT-I12TBT, however this is not the goal of this study. Rather we focus on explaining how the side chain length affects the morphology in this material class. The MC with the branched side chain IHDTBT exhibited the worst device performance in spite of the most favorable absorbance.

Table 1: Best performance data of I*n*TBT:PCBM OPVs in the standard device setup (composition 2:3).

Merocyanine	V_{OC} (V)	J_{sc} (mA/cm^2)	FF	PCE (%)
I6TBT	0.76 ± 0.01	8.29 ± 0.38	0.52 ± 0.02	3.3 ± 0.1
I7TBT	0.89 ± 0.01	6.95 ± 0.15	0.63 ± 0.01	3.9 ± 0.1
I8TBT	0.89 ± 0.01	7.90 ± 0.24	0.64 ± 0.02	4.5 ± 0.1
I9TBT	0.90 ± 0.01	7.83 ±0.22	0.64 ± 0.02	4.5 ± 0.1
I10TBT	0.90 ± 0.01	7.28 ± 0.13	0.65 ± 0.01	4.3 ± 0.1
I11TBT	0.90 ± 0.01	6.69 ± 0.28	0.67 ± 0.01	4.0 ± 0.1
I12TBT	0.86 ± 0.01	6.20 ± 0.3	0.63 ± 0.02	3.4 ± 0.3
IHDTBT	0.79 ± 0.01	2.03 ± 0.06	0.37 ± 0.02	0.6 ± 0.1

To probe the smallest length scale structures (Å) in pure InTBT and 2:3 InTBT:PCBM films we use grazing incidence x-ray diffraction (GIXRD) (Figures: S7 − S23). Diffraction peaks were fit with a Pseudo-Voigt model to extract peak positions and widths.[30,31] Bragg's Law was used to calculate crystal d-spacing and the Scherrer equation was used to calculate coherence length (L_C) for the most prominent InTBT and PCBM peaks (Tables: 2, S19).[32–34] GIXRD of the pure PCBM film shows two peaks at 2θ ∼19.5° and ∼9.7°, in accordance with literature.[35]

In the pure InTBT films, the samples with side chains $n \leq 8$ form larger crystals with L_C ($>$ 14 nm) (Table: 2). In InTBT samples with side chain $n \geq 9$ (and IHDTBT) the side chain is long enough to impede crystal growth, thereby reducing the L_C ($<$ 8.2 nm). In the InTBT:PCBM films, the InTBT L_C decreases significantly in all of the studied samples suggesting that InTBTs form smaller more disordered crystals when mixed with PCBM (Table: 2). The L_C of the PCBM peak at 2θ ∼19.5° remains consistent (∼ 1.6 nm) in all of the InTBT:PCBM films (Table: S19), which shows that pure PCBM crystalline domains form in all films. The ratio of the prominent InTBT to PCBM peak intensity in the mixed films are shown in Figure 4. InTBTs with $n \leq 8$ and n =HD form pure InTBT crystalline domains in the presence of PCBM. Their prominent diffraction peak intensity around ∼7.5° are 2 to 6 times greater then their corresponding PCBM peak intensity. As the linear side chain is increased to $n \geq 9$, the InTBT peaks broaden significantly and the prominent peak height ratio ($\frac{\text{I}n\text{TBT Peak Height}}{\text{PCBM Peak Height}}$) decreases below unity (Figures: 4 and S14-S21). A similar drop in the prominent peak integration ratio ($\frac{\text{I}n\text{TBT Peak Integration}}{\text{PCBM Peak Integration}}$) is observed, although the change is less discernible due to the broadening of the InTBT diffraction peaks and the large FWHM of the PCBM peak. This suggests that InTBTs with linear side chains $n \geq 9$ undergo significant mixing with PCBM and form amorphous structures that do not have long range order.

InTBT diffraction peaks for n $\leq$ 8 broaden and shift when mixed with PCBM resulting in minor shifts in the prominent InTBT d-spacing (Table 2). I6TBT d-spacing decreases from 12.0 to 11.5 Å while both I7TBT and I8TBT d-spacings increase from 11.1 and 12.6 to 12.5 and 12.8 Å respectively. More significant changes upon mixing are observed for I*n*TBTs with n ≥ 9. The I9TBT peaks at $2\theta =$ 4.64°, 5.31°, 7.06°, and 9.11° merge into a single broad peak at 7.63° when mixed with PCBM resulting in the apparent I*n*TBT:PCBM d-spacing of 11.6 Å. The I10TBT peaks at 7.16° and 8.66° merge into the broad peak at 7.95° when mixed with PCBM resulting in the apparent I*n*TBT:PCBM d-spacing of 11.1 Å. Upon mixing with PCBM, I11TBT peaks broaden and merge but are still distinguishable; the peaks at 4.25° and 5.05° shift to 4.02° and 4.95°, increasing the d-spacing to 22 and 17.8 Å respectively. The peaks at 7.19° and 8.49° shift to 7.27° and 8.24° changing the d-spacing to 12.2 and 10.7 Å. The I12TBT peaks at 4.04° and 4.93° merge into the broad peak at 4.26° when mixed with PCBM resulting in the apparent I12TBT:PCBM d-spacing of 20.7 Å. Finally, upon mixing with PCBM the IHDTBT peak shifts from 4.25° to 4.18° resulting in a d-spacing 21.2 Å. In summary, when mixed with PCBM the I*n*TBTs with n ≤ 8 remain phase segregated and show minor broadening and shifting of their prominent diffraction peaks. While I*n*TBTs with n ≥ 9 allow intercalation of PCBM into the I*n*TBT crystals causing significant broadening of their diffraction peaks due to reduced long range order.

Table 2: Bragg's d-spacing and Scherrer's coherence length L_C extracted from most prominent I*n*TBT peak (in the range of $2\theta \sim$4-10°) from pure and mixed I*n*TBT:PCBM films.

I*n*TBT	I*n*TBT d-Spacing (Å)	I*n*TBT L_C (Å)	I*n*TBT:PCBM d-Spacing (Å)	I*n*TBT:PCBM L_C (Å)
I6TBT	12.0 ± 0.1	147 ± 2	11.5 ±0.1	41 ± 1
I7TBT	11.1 ± 0.1	220 ± 6	12.5 ± 0.1	75 ± 8
I8TBT	12.6 ± 0.1	181 ± 8	12.8±0.1	87 ± 6
I9TBT	9.7 ± 0.1	56 ± 37	11.6±0.1	11 ± 8
I10TBT	10.2 ± 0.1	39 ± 8	11.1±0.1	17 ± 15
I11TBT	17.5 ± 0.1	82 ± 4	17.8±0.1	42 ± 4
I12TBT	17.9 ± 0.1	40 ± 6	20.7±0.1	39 ± 25
IHDTBT	20.8 ± 0.1	82 ± 3	21.1±0.1	48 ± 27

We use SANS to probe the size, shape, and composition of nanoscale (3-200 nm) domains in I*n*TBT:PCBM films (7 ≤ n ≥ 11).[36] Differences in the ^{1}H density between I*n*TBT and

PCBM lead to a neutron scattering contrast. Figure 5 (a) shows SANS data (I(Q) vs Q), where I is intensity and Q is momentum transfer in units of $\mathrm{\AA}^{-1}$. This scattering data is fit to a model that determines statistical length scale correlations and relative density differences between domains. SANS is not sensitive to crystallinity, which allows us to probe structural and compositional density distributions of the full bulk sample, not just the crystalline regions as for x-ray diffraction analysis.

The I*n*TBTs with linear side chains form elongated domains that are best fit with an ellipsoidal form factor.[37] We therefore use a model that assumes elongated I*n*TBT rich domains surrounded by PCBM rich material. Figure 5 (b) depicts the parameters extracted from the fit, where R_S is the mean radius along the short axis of the ellipsoid, R_L is the mean radius along the long axis of the ellipsoid, and the scattering length density (SLD) contrast is a parameter describing the compositional difference between the ellipsoids and surrounding matrix. The lognormal domain size-dispersity (SD) of R_S and R_L is displayed in Figures S24 and S25.

From the previously discussed GIXRD, I7TBT and I8TBT MCs form pure crystalline phases when mixed with PCBM. Since the SLD for neutrons depends on the atomic density and composition of each phase, the ellipsoid SLDs (Table S20) are estimated from unit cell information obtained from single crystal simulations (Table S2). The SLD of a pure crystalline PCBM domain is also shown in Table S20.[38] The expected SLD contrast for pure I*n*TBT and PCBM domains is 3.3-3.4 $\times 10^{-6}$ $\mathrm{\AA}^{-2}$. Since the measured SLD contrast between the ellipsoidal I*n*TBT domains and the surrounding matrix is much smaller than expected for pure domains ($\sim 1.2 \times 10^{-6}$ $\mathrm{\AA}^{-2}$) and since PCBM forms pure clusters that are too small to be detected with SANS (Table S19), the matrix is assumed to be a mixed I*n*TBT:PCBM domain. For I7TBT and I8TBT, the total volume fraction of the ellipsoidal domains ($\phi_{Ellipsoid}$) are determined with Equations **??** and S7 (Table 3), where the partial volume fractions of PCBM and I*n*TBT are known from solution concentrations. As the linear I*n*TBT side chain is increased from 7 to 8 carbons R_S decreases from 5.3 ± 0.1 to 3.0 ± 0.5

nm and R_L remains consistent at 13.5 ±0.4 and 13.4 ± 0.6 nm respectively. So the needle length is maintained but the diameter narrowed. I8TBT also has more InTBT dispersed in the mixed phase as seen in the decreased SLD contrast from 1.26 to 1.18 $\times 10^{-6}$Å^{-2}. This means that I8TBT has a reduced volume percent of ellipsoidal InTBT domains of 26% compared to 28% for I7TBT.

As shown by GIXRD, InTBTs with linear side chains $n \geq 9$ allow PCBM to intercalate into the InTBT crystalline domains resulting in a further reduction in the SLD contrast. Thus the model now corresponds to mixed InTBT-rich InTBT:PCBM ellipsoids in a matrix of amorphous PCBM-rich mixed domain. As the linear InTBT side chain is increased from 9 to 10 carbons, R_L increases from 15.6 ± 1.5 to 21.8 ± 0.5 nm and R_S remains consistent at 4.3 ± 0.2 and 4.2 ± 0.2 nm respectively. So the mixed crystalline InTBT:PCBM needles become longer while maintaining roughly the same diameter as I8TBT and I7TBT. Interestingly, the I11TBT sample contained the largest ellipsoids in both dimensions with a R_S of 7.1 ± 0.1 nm and an R_L of 23.1 ± 0.5 nm. All of the InTBT films show an increasing scattering intensity through the low Q detector limit. The slope of the intensity increase at low Q follows Porod's Law[39] which suggests the presence of larger structures ($>$ 200 nm) in the films that are outside our instruments measurement range.

SANS data was also collected for IHDTBT:PCBM. The intensity profile was best fit to two models (Figure S26). A spherical form factor was fit to the bend in the spectrum at Q=.05 Å^{-1} and a fuzzy sphere (FS) form factor was fit to the low Q intensity, the combined fit is shown in Figure 5.[37] The spherical radius is 4.8 ± 0.2 nm, plotted as R_S, and the mean FS radius is 52.2 ± 0.2 nm, plotted as R_L. The surface of the FS is smeared with a Gaussian to obtain a gradual drop off in SLD, the width of the smeared surface interface is 3.7 ± 0.3 nm. Similar to the InTBTs with linear side chains, IHDTBT forms a distribution of domain sizes ranging from 20 - 80 nm (Figure S27). IHDTBT:PCBM films are more phase segregated resulting in the increased SLD contrast between the FS and the surrounding matrix of 1.89×10^{-6} Å^{-2}.

Table 3: Volume fraction of I7TBT and I8TBT in ellipsoidal and mixed domains obtained from SANS fits, and volume fraction of PCBM in mixed domains from sample preparation.

Merocyanine	$\Phi^{InTBT}_{Ellipsoid}$	Φ^{InTBT}_{Mixed}	Φ^{PCBM}_{Mixed}
I7TBT	0.28	0.21	0.52
I8TBT	0.26	0.24	0.50

We use AFM to study the mesoscale (25 nm$-$ 5 μm) surface structures on InTBT:PCBM films ($7 \leq n \leq 11$, and $n =$ HD). Figure 6 (a) depicts the height profile and root mean square roughness (R_{MS}) of the films. I7TBT:PCBM and IHDTBT:PCBM have the largest R_{MS} of 10.1 $\pm$0.5 nm and 7.3 $\pm$0.5 nm respectively. These films exhibit depressions in the surface that dig $> 50\%$ down into the 70 nm films. This is in agreement with SANS and GIXRD; I7TBT and IHDTBT phase segregate when mixed with PCBM resulting in increased surface roughness. The I7TBT:PCBM surface shows a connected network of elongated domains with lateral size variations 200 ± 110 nm, while the IHDTBT surface shows round unconnected domains on the order of 240 ± 80 nm. I8TBT:PCBM film surface forms elongated domains (on the size of 210 ± 100 nm) that are less pronounced than the I7TBT:PCBM film and has an R_{MS} of 5.2 $\pm$0.5 nm. The similar domain size but reduced fraction of InTBT domains is consistent with the SANS analysis of I7TBT:PCBM and I8TBT:PCBM. Pure InTBT crystals are still present as the side chain is increased to $n = 8$ but the longer side chain begins to reduce mesoscopic phase segregation. In accordance with GIXRD and SANS, the I9TBT:PCBM, I110TBT:PCBM and I11TBT:PCBM films form large mixed domains that result in a low R_{MS} of 2.6 $\pm$0.5, 3.9 $\pm$0.5, and 3.6 $\pm$0.5 nm respectively.

The phase images provide finer detail of the surface composition. Figure 6 (b) shows the corresponding AFM phase images. It is clear that the phase domains for I7TBT:PCBM, I11TBT:PCBM, and IHDTBT:PCBM directly correlate to features observed in the height images. Since I7TBT:PCBM and IHDTBT:PCBM films have the roughest surface topography and the phase shift has a pattern of increasing and decreasing($\pm 10^\circ$ for I7TBT and $\pm 7.5^\circ$ for IHDTBT) on the edges of raised surface domains, the observed phase shift is likely an instrument artifact; the tapping AFM tip phase shifts as the tip travels up over a raised surface domain and shifts in the opposite direction as the tip travels down into a depression in the film surface. For this reason we choose to exclude those films from the following phase analysis. This is not observed in the I11TBT:PCBM film due to its lower surface roughness. For I11TBT:PCBM the raised domains in the height image are compositionally different from the surrounding film. Figure 7 compares the mean grain sizes extracted from the phase images and R_{MS} from height images. The grains are defined by a cutoff phase shift. Red grains have $> 4°$ phase shift, corresponding to I*n*TBT-rich domains, and blue grains have $< -4°$ phase shift, corresponding to PCBM-rich domains. Figure 7 depicts mean blue (PCBM-rich) and red (I*n*TBT-rich) grain size; grain size distributions are shown in Figures S28 and S29. Starting with the shortest side chain film the I8TBT phase image shows networks of interconnected domains resulting in the relatively large mean PCBM-rich grain size of 630 nm^2, and a mean I*n*TBT-rich grain size of 500 nm^2. As the side chain is increased, I9TBT forms domains with reduced connectivity resulting in mean PCBM-rich and I*n*TBT-rich grain sizes of 160 and 650 nm^2 respectively. I10TBT forms a well mixed film surface resulting the smoothest phase images with mean PCBM-rich and I*n*TBT-rich grain sizes of 80 and 230 nm^2. As the side chain is increased further, the I11TBT films begin to form large disconnected domains with mean PCBM-rich and I*n*TBT-rich grain sizes of 560 and 1540 nm^2.

4 Discussion

This series of I*n*TBTs with varying linear side chain length demonstrate the morphologically controlled balance between exciton dissociation, charge carrier transport, and recombination. A generated exciton can diffuse up to 10 nm before geminate recombination (GR) occurs.[40,41] Charge separation is maximized when I*n*TBT domain size is minimized to increase the probability of an exciton being generated within 5-10 nm of a I*n*TBT/PCBM interface.[40,41] However there is a necessary balance between exciton dissociation and free charge carrier transport. Small disconnected InTBT domains reduce hole transport through the film and increase trap sites for free charge carriers increasing nongeminate recombination (NGR) rates.[42]

Figure 8 illustrates the bulk morphologies reported by GIXRD and SANS for I8TBT:PCBM, I9TBT:PCBM, and I11TBT:PCBM. The PCBM coherence length remains constant at 1.6 nm. I8TBT:PCBM films form pure MC ellipsoids (R_S = 3 nm, R_L = 14 nm) composed of crystalline MC domains with a large MC coherence length (8.7 nm), that are surrounded by a mixed MC:PCBM domain. I9TBT:PCBM films form larger mixed ellipsoids (R_S = 4 nm, R_L = 16 nm) with a shorter MC coherence length (1.1 nm), also surrounded by a mixed MC:PCBM domain. Finally, I11TBT:PCBM films form even larger, more mixed ellipsoids (R_S = 7 nm, R_L = 23 nm), composed of MC crystalline regions with increased coherence length (4.2 nm).

GIXRD shows that I6TBT through I8TBT form pure crystalline phases in InTBT:PCBM films. When the side chain length is increased to $n \geq 9$, PCBM mixes with InTBT significantly broadening the observed diffraction peaks. Of the InTBTs with linear side chains, I6TBT:PCBM films have the lowest FF and V_{OC}. GIXRD demonstrates the presence of small unmixed I6TBT domains (L_C = 4.1 nm) which results in high geminate recombination rates. Since our BHJs were fabricated with a 2:3 InTBT:PCBM weight fraction and I6TBT has the lowest molecular weight out of the studied materials, BHJs with I6TBT have the highest molar ratio of InTBT to PCBM. This resulted in a stronger absorbance and the highest J_{SC} of 8.29 $\frac{mA}{cm^2}$. Likewise, I12TBT:PCBM films have the lowest molar ratio of InTBT to PCBM resulting in the lowest J_{SC} of 6.20 $\frac{mA}{cm^2}$. GIXRD shows that the 12 carbon linear side chain on I12TBT allows strong mixing between I12TBT and PCBM, which resulted in lower V_{OC} and FF. Since BHJs with I6TBT and I12TBT show reduced PCE due to little and too much mixing respectively, we chose to exclude I6TBT and I12TBT from further morphological analysis.

I7TBT and I8TBT BHJs have the same V_{OC}= 0.89 V. They both form pure crystalline domains when mixed with PCBM with a L_C of 7.5 and 8.7 nm respectively. The SANS data shows R_L of $\sim$5 nm for all films, which should mean that all excitons can reach a donor/acceptor interface, minimizing GR. The topography of the I7TBT:PCBM film shows a larger surface roughness than I8TBT:PCBM due to decreased miscibility. The I8TBT:PCBM film has fewer pure InTBT domains and more InTBT in the mixed phase leading to increases in J_{SC} and FF. Finally the I8TBT:PCBM film has the highest PCE of 4.5%, due to a combination of high J_{SC} and FF.

OPV devices with I9TBT, I10TBT, and I11TBT have the same $V_{OC} = 0.90$ V. They do not form pure crystalline domains when mixed with PCBM and have a much lower coherence length than I7TBT or I8TBT BHJs for both InTBT and PCBM rich domains. Curiously, in spite of the increased domain size and the onset of InTBT:PCBM mixing with increased side chain length, the JV characteristics show a remarkably consistent and smooth trend in device characteristics with V_{OC} peaking for $n = 9 - 11$, J_{SC} peaking for $n = 8$, and FF peaking for $n = 11$. Thus I9TBT:PCBM films also produce the highest PCE of 4.5%, even though GIXRD and AFM show they form an entirely different structural motif compared to I8TBT:PCBM films. SANS demonstrates InTBTs with $n \geq 9$ form ellipsoidal InTBT domains with reduced SLD contrast due to the presence of PCBM in both the ellipsoid and the surrounding matrix. The J_{SC} decreases with $n > 8$ because the increased side chain length effectively means lower absorption coefficient for the 2:3 InTBT:PCBM film. The increase of FF with increased n may be due to a relative v% increase in acceptor.[43]

In spite of the most favorable absorbance, the branched side IHDTBT:PCBM device exhibited the worst OPV performance due to unfavorable morphology across several orders of magnitude. GIXRD shows the long branched side chains inhibit intercalation of the PCBM into IHDTBT domains. This is confirmed by the increased SLD contrast from SANS. It should be noted that an increased SLD contrast is also caused by increased ^{1}H density on the longer side chains. SANS demonstrates the presence of small $\sim$10 nm IHDTBT domains however both SANS and AFM show IHDTBT forms large pure domains on the order of

100-240 nm significantly increasing the geminate recombination rates which results in the low J_{SC} of 2.03 $\frac{mA}{cm^2}$ and PCE of 0.6%.

It is useful to speculate what the device optimization and morphology assessment performed here indicates about the device efficiency limits for InTBT:PCBM OPVs. V_{OC} is quite high at 0.9 V and essentially the same for all linear InTBTs, therefore it does not need to be optimized. Our analysis fixed the OPV layer thickness at 70 nm and wt. ratio of InTBT:PCBM at 2:3 because these parameters came from a prior optimization of MC:PCBM solubility.[27] The trend in FF indicates that the hole and electron currents are well balanced with little bimolecular recombination in films up to 70 nm device thickness. With such high FF and no optimization of the mixing ratio, it is likely that layer thicknesses of up to $\sim$ 200 nm would still have FF above 0.6. Given the absorbance up to $\sim$ 725 nm (which is $\sim$ 1.7 eV) one could expect J_{SC} of up to 15 $\frac{mA}{cm^2}$ under AM1.5 illumination and an optimized PCE of 6.5-8%.[44]

Another intriguing series of future experiments should focus on mixing multiple different InTBTs with fullerenes. Since the InTBTs form mixed structures for $n \geq 9$ and $n \leq 8$ form pure domains, one could exert far more control over the morphology using a combination of InTBTs with mixed side chain lengths to obtain even greater improvements to the FF.

Although PCEs reported in this manuscript could be considered relatively low compared to recent record small molecule devices, we point out that D-A MC dyes are extremely inexpensive. Previous small molecule OPV studies claim that D-A-D like structures are needed to prevent dipole alignment between neighboring molecules in order to obtain high PCEs. However, we demonstrate that decent PCEs can be obtained through morphological optimization of D-A systems and that the miscibility with a PCBM acceptor can be tuned through a range of domain sizes and mixing ratios.

5 Conclusions

This manuscript demonstrates a novel series of MC dyes with varying hydrocarbon side chain length. BHJ OPV devices were fabricated with 2:3 wt. ratio InTBT:PCBM and characterized as a function of side chain length. A maximum PCE of 4.5 ± 0.1% was extracted from I8TBT:PCBM and I9TBT:PCBM devices. As expected, tuning the side chain length allows careful adjustment of the miscibility between the donor and acceptor, thereby enabling optimization of film morphology and OPV performance characteristics. Hierarchical structure formation was studied using GIXRD (Å), SANS (3-200 nm), and AFM (25 nm$-$ 5 μm). When mixed with PCBM, InTBTs with ≤ 8 side chain carbons form pure crystalline domains, while InTBTs with ≥ 9 side chain carbons form mixed domains with PCBM. SANS demonstrates that increasing side chain length increases InTBT-rich domain size while at the same time allowing for mixed domains for n ≥ 9. The branched side chain IHDTBT:PCBM film was also studied and was found to exhibit the worst performance OPV device, the large side chain inhibited mixing between IHDTBT and PCBM resulting in large segregated phases. Further optimization of the mixing ratios and layer thickness could nearly double the OPV performance. Ternary mixtures of InTBTs with different side chain length could enable even more control over BHJ morphology.

6 Acknowledgments

This project was supported by the U.S. Department of Energy, Office of Basic Energy Sciences, Division of Materials Sciences and Engineering, under Award No. DE-SC0010419, and the German Federal Office of Science and Technology (BMBF, MEDOS FKZ: 03EK3505I). Thanks to the Alexander von Humboldt Foundation and to the Universität zu Köln alumni fellowship fund. for sabbatical funding for A.J.M.. Thanks to the Jülich Centre for Neutron Science at Heinz Maier-Leibnitz Zentrum in Garching, Germany for Small-Angle Neutron Scattering measurement time. This work benefited from the use of the SasView application, originally developed under NSF award DMR-0520547. SasView contains code developed with funding from the European Unions Horizon 2020 research and innovation programme under the SINE2020 project, grant agreement No 654000

7 Conflicts of Interest

There are no conflicts of interest to declare.

References

(1) Roncali, J.; Leriche, P.; Blanchard, P. Molecular Materials for Organic Photovoltaics: Small is Beautiful. *Adv. Mater.* **2014**, *26*, 3821–3838.

(2) Augulis, R.; Devizis, A.; Peckus, D.; Gulbinas, V.; Hertel, D.; Meerholz, K. High Electron Mobility and Its Role in Charge Carrier Generation in Merocyanine/Fullerene Blends. *J. Phys. Chem. C* **2015**, *119*, 5761–5770.

(3) Arjona-Esteban, A.; Krumrain, J.; Liess, A.; Stolte, M.; Huang, L.; Schmidt, D.; Stepanenko, V.; Gsanger, M.; Hertel, D.; Meerholz, K.; Wurthner, F. Influence of Solid-State Packing of Dipolar Merocyanine Dyes on Transistor and Solar Cell Performances. *J. Am. Chem. Soc.* **2015**, *137*, 13524–13534.

(4) Nils M. Kronenberg, M. D. F. W. K. M., Hannah Bürckstümmer Optimized solution-processed merocyanine:PCBM organic bulk heterojunction solar cell. *J. Photonics Energy* **2011**, *1*, 1 – 8 – 8.

(5) Ghosh, A. K.; Feng, T. Merocyanine organic solar cells. *J. Appl. Phys.* **1978**, *49*, 5982–5989.

(6) Wrthner, F.; Meerholz, K. Systems Chemistry Approach in Organic Photovoltaics. *Chemistry A European Journal* **2010**, *16*, 9366–9373.

(7) Mishra, A.; Bauerle, P. Small Molecule Organic Semiconductors on the Move: Promises for Future Solar Energy Technology. *Angew. Chem. Int. Ed.* **2012**, *51*, 2020–2067.

(8) Lin, Y.; Li, Y.; Zhan, X. Small molecule semiconductors for high-efficiency organic photovoltaics. *Chem. Soc. Rev.* **2012**, *41*, 4245–4272.

(9) Li, Y.; Guo, Q.; Li, Z.; Pei, J.; Tian, W. Solution processable D-A small molecules for bulk-heterojunction solar cells. *Energy Environ. Sci.* **2010**, *3*, 1427–1436.

(10) Liess, A.; Arjona-Esteban, A.; Kudzus, A.; Albert, J.; Krause, A.-M.; Lv, A.; Stolte, M.; Meerholz, K.; Wrthner, F. Ultranarrow Bandwidth Organic Photodiodes by Exchange Narrowing in Merocyanine H- and J-Aggregate Excitonic Systems. *Advanced Functional Materials* **2019**, *29*, 1805058.

(11) Kronenberg, N. M.; Deppisch, M.; Würthner, F.; Lademann, H. W. A.; Deing, K.; Meerholz, K. Bulk heterojunction organic solar cells based on merocyanine colorants. *Chem. Commun.* **2008**, 6489–6491.

(12) Steinmann, V.; Kronenberg, N. M.; Lenze, M. R.; Graf, S. M.; Hertel, D.; Bürckstümmer, H.; Würthner, F.; Meerholz, K. A simple merocyanine tandem solar cell with extraordinarily high open-circuit voltage. *Appl. Phys. Lett.* **2011**, *99*, 193306.

(13) Steinmann, V.; Kronenberg, N. M.; Lenze, M. R.; Graf, S. M.; Hertel, D.; Meerholz, K.; Bürckstümmer, H.; Tulyakova, E. V.; Würthner, F. Simple, Highly Efficient Vacuum-Processed Bulk Heterojunction Solar Cells Based on Merocyanine Dyes. *Adv. Energy Mater.* **2011**, *1*, 888–893.

(14) Bürckstümmer, H.; Tulyakova, E. V.; Deppisch, M.; Lenze, M. R.; Kronenberg, N. M.; Gsanger, M.; Stolte, M.; Meerholz, K.; Würthner, F. Efficient Solution-Processed Bulk Heterojunction Solar Cells by Antiparallel Supramolecular Arrangement of Dipolar Donor-Acceptor Dyes. *Angew. Chem. Int. Ed.* **2011**, *50*, 11628–11632.

(15) Gräß er, N.; Wolf, S.; Holzmüller, F.; Zeika, O.; Vandewal, K.; Leo, K. Heteroquinoid Merocyanine Dyes with High Thermal Stability as Absorber Materials in Vacuum-Processed Organic Solar Cells. *Eur. J. Org. Chem.* **2019**, *2019*, 845–851.

(16) Wang, Z.; Zhu, L.; Shuai, Z.; Wei, Z. A-π-D-π-A Electron-Donating Small Molecules for Solution-Processed Organic Solar Cells: A Review. *Macromol. Rapid Commun.* **2017**, *38*, 1700470.

(17) Zhou, R.; Jiang, Z.; Yang, C.; Yu, J.; Feng, J.; Adil, M. A.; Deng, D.; Zou, W.; Zhang, J.; Lu, K.; Ma, W.; Gao, F.; Wei, Z. All-small-molecule organic solar cells with over 14morphologies. *Nat. Commun.* **2019**, *10*, 5393.

(18) Menke, S. M.; Holmes, R. J. Exciton diffusion in organic photovoltaic cells. *Energy Environ. Sci.* **2014**, *7*, 499–512.

(19) Hestand, N. J.; Spano, F. C. Expanded Theory of H- and J-Molecular Aggregates: The Effects of Vibronic Coupling and Intermolecular Charge Transfer. *Chem. Rev.* **2018**, *118*, 7069–7163, PMID: 29664617.

(20) Chang, M.; Meng, L.; Wang, Y.; Ke, X.; Yi, Y.-Q.-Q.; Zheng, N.; Zheng, W.; Xie, Z.; Zhang, M.; Yi, Y.; Zhang, H.; Wan, X.; Li, C.; Chen, Y. Achieving an Efficient and Stable Morphology in Organic Solar Cells Via Fine-Tuning the Side Chains of Small-Molecule Acceptors. *Chem. Mater.* **2020**, *32*, 2593–2604.

(21) Qiu, B.; Chen, S.; Xue, L.; Sun, C.; Li, X.; Zhang, Z.-G.; Yang, C.; Li, Y. Effects of Alkoxy and Fluorine Atom Substitution of Donor Molecules on the Morphology and Photovoltaic Performance of All Small Molecule Organic Solar Cells. *Front. Chem.* **2018**, *6*, 413.

(22) Jurow, M. J.; Hageman, B. A.; DiMasi, E.; Nam, C.-Y.; Pabon, C.; Black, C. T.; Drain, C. M. Controlling morphology and molecular packing of alkane substituted ph-

thalocyanine blend bulk heterojunction solar cells. *J. Mater. Chem. A* **2013**, *1*, 1557–1565.

(23) Krause, L.; Herbst-Irmer, R.; Sheldrick, G. M.; Stalke, D. Comparison of silver and molybdenum microfocus X-ray sources for single-crystal structure determination. *J. Appl. Crystallogr.* **2015**, *48*, 3–10.

(24) Sheldrick, G. M. *SHELXT* – Integrated space-group and crystal-structure determination. *Acta Crystallographica Section A* **2015**, *71*, 3–8.

(25) Elschner, C.; Levin, A. A.; Wilde, L.; Grenzer, J.; Schroer, C.; Leo, K.; Riede, M. Determining the C60 molecular arrangement in thin films by means of X-ray diffraction. *J. Appl. Crystallogr.* **2011**, *44*, 983–990.

(26) Kronenberg, N. M.; Steinmann, V.; Bürckstümmer, H.; Hwang, J.; Hertel, D.; Würthner, F.; Meerholz, K. Direct Comparison of Highly Efficient Solution- and Vacuum-Processed Organic Solar Cells Based on Merocyanine Dyes. *Adv. Mater.* **2010**, *22*, 4193–4197.

(27) Lenze, M. R.; Kronenberg, N. M.; Würthner, F.; Meerholz, K. In-situ modification of PEDOT:PSS work function using alkyl alcohols as secondary processing solvents and their impact on merocyanine based bulk heterojunction solar cells. *Org. Electron.* **2015**, *21*, 171 – 176.

(28) Qi, B.; Wang, J. Fill factor in organic solar cells. *Phys. Chem. Chem. Phys.* **2013**, *15*, 8972–8982.

(29) Jao, M.-H.; Liao, H.-C.; Su, W.-F. Achieving a high fill factor for organic solar cells. *J. Mater. Chem. A* **2016**, *4*, 5784–5801.

(30) Sánchez-Bajo, F.; Cumbrera, F. L. The Use of the Pseudo-Voigt Function in the Vari-

ance Method of X-ray Line-Broadening Analysis. *J. Appl. Crystallogr.* **1997**, *30*, 427–430.

(31) Olivero, J.; Longbothum, R. Empirical fits to the Voigt line width: A brief review. *J. Quant. Spectrosc. Radiat. Transfer* **1977**, *17*, 233 – 236.

(32) Bragg, W. H.; Bragg, W. L. The reflection of X-rays by crystals. *Proceedings of the Royal Society of London. Series A, Containing Papers of a Mathematical and Physical Character* **1913**, *88*, 428–438.

(33) Patterson, A. L. The Scherrer Formula for X-Ray Particle Size Determination. *Phys. Rev.* **1939**, *56*, 978–982.

(34) Rivnay, J.; Noriega, R.; Kline, R. J.; Salleo, A.; Toney, M. F. Quantitative analysis of lattice disorder and crystallite size in organic semiconductor thin films. *Phys. Rev. B* **2011**, *84*, 045203.

(35) Mens, R.; Chambon, S.; Bertho, S.; Reggers, G.; Ruttens, B.; D'Haen, J.; Manca, J.; Carleer, R.; Vanderzande, D.; Adriaensens, P. Description of the nanostructured morphology of [6,6]-phenyl-C61-butyric acid methyl ester (PCBM) by XRD, DSC and solid-state NMR. *Magn. Reson. Chem.* **2011**, *49*, 242–247.

(36) Toyoko Imae, M. F. N. T., Toshiji Kanaya *Neutrons in Soft Matter*; Wiley, 2011.

(37) L. A. Feigin, D. I. S. In *Structure Analysis by Small-Angle X-Ray and Neutron Scattering*; Taylor, G. W., Ed.; Springer, 1987.

(38) Clulow, A. J.; Armin, A.; Lee, K. H.; Pandey, A. K.; Tao, C.; Velusamy, M.; James, M.; Nelson, A.; Burn, P. L.; Gentle, I. R.; Meredith, P. Determination of Fullerene Scattering Length Density: A Critical Parameter for Understanding the Fullerene Distribution in Bulk Heterojunction Organic Photovoltaic Devices. *Langmuir* **2014**, *30*, 1410–1415.

(39) Sinha, S. K.; Sirota, E. B.; Garoff, S.; Stanley, H. B. X-ray and neutron scattering from rough surfaces. *Phys. Rev. B* **1988**, *38*, 2297–2311.

(40) Dou, L.; You, J.; Hong, Z.; Xu, Z.; Li, G.; Street, R. A.; Yang, Y. 25th Anniversary Article: A Decade of Organic/Polymeric Photovoltaic Research. *Adv. Mater.* **2013**, *25*, 6642–6671.

(41) Wojcik, M.; Nowak, A.; Seki, K. Geminate electron-hole recombination in organic photovoltaic cells. A semi-empirical theory. *The Journal of Chemical Physics* **2017**, *146*, 054101.

(42) Gohler, C.; Wagenpfahl, A.; Deibel, C. Nongeminate Recombination in Organic Solar Cells. *Adv. Electron. Mater.* **2018**, *4*, 1700505.

(43) Moulé, A. J.; Bonekamp, J. B.; Meerholz, K. The effect of active layer thickness and composition on the performance of bulk-heterojunction solar cells. *J. Appl. Phys.* **2006**, *100*, 094503.

(44) Scharber, M.; Mhlbacher, D.; Koppe, M.; Denk, P.; Waldauf, C.; Heeger, A.; Brabec, C. Design Rules for Donors in Bulk-Heterojunction Solar CellsTowards 10% Energy-Conversion Efficiency. *Adv. Mater.* **2006**, *18*, 789–794.

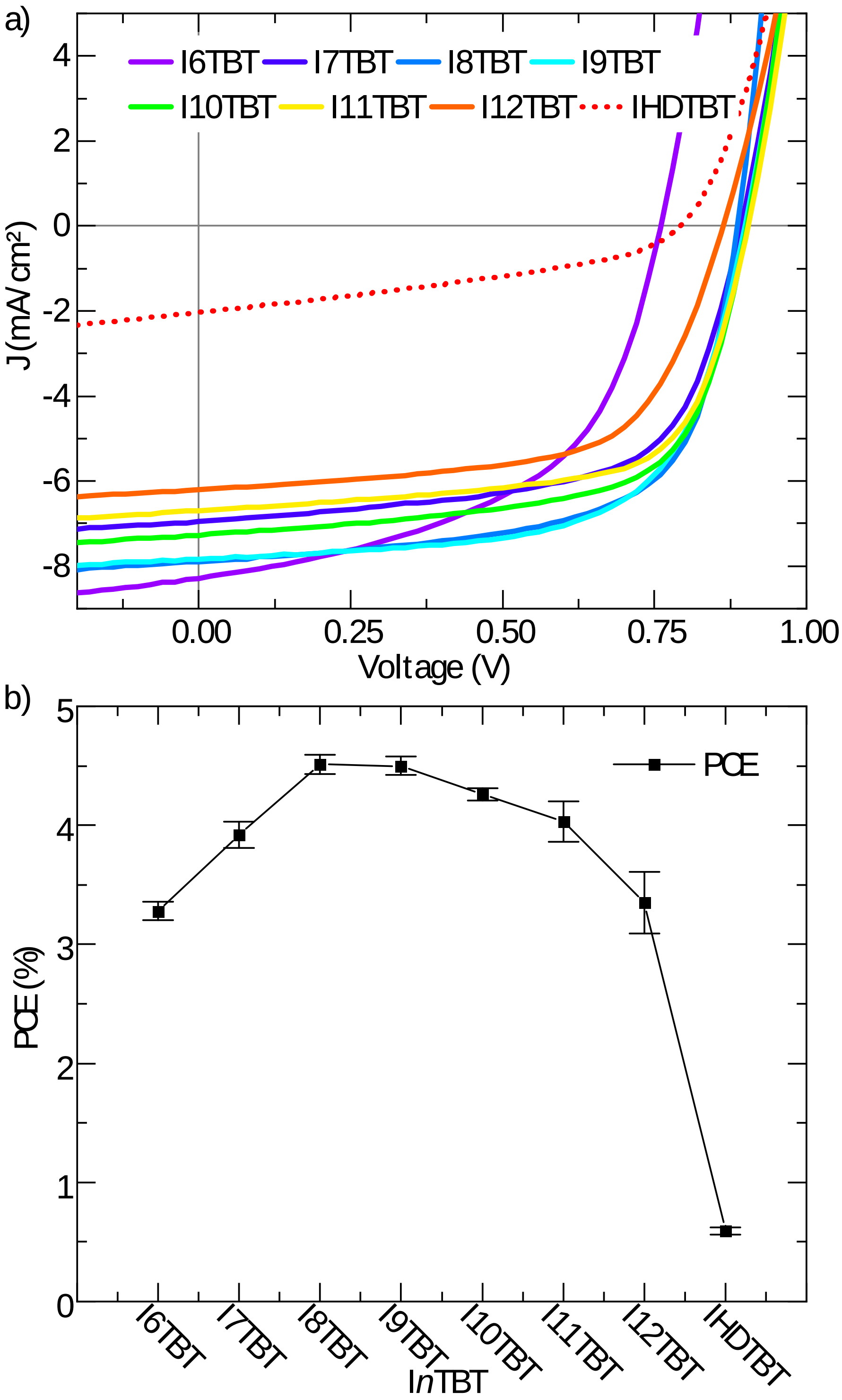

Figure 3: (a) JV curves and (b) extracted power conversion efficiencies from 3:2 by wt. InTBT:PCBM devices.

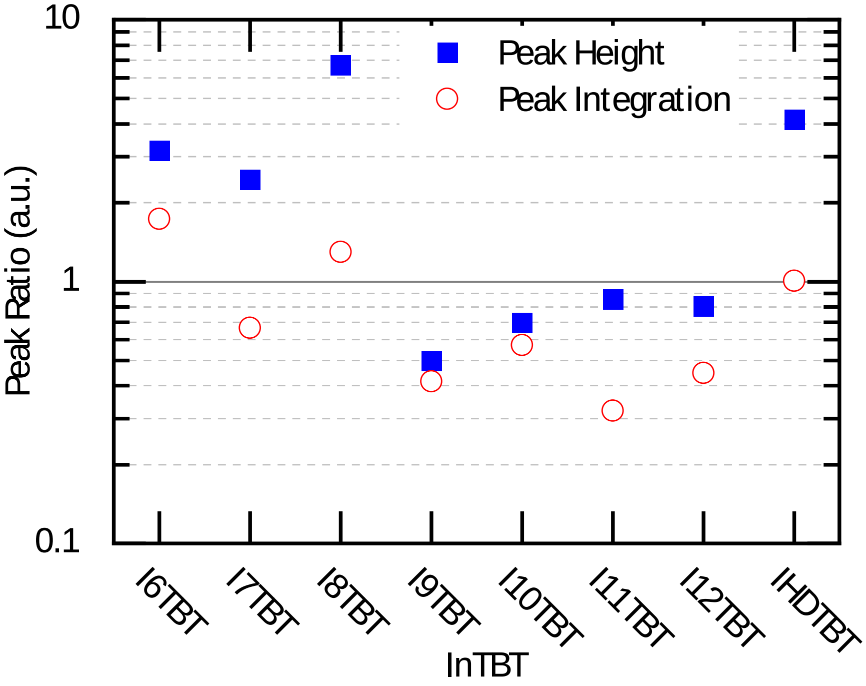

Figure 4: GIXRD: Ratio of prominent InTBT peak over prominent PCBM peak (peak heights and peak integrations) in mixed 3:2 by wt. InTBT:PCBM films.

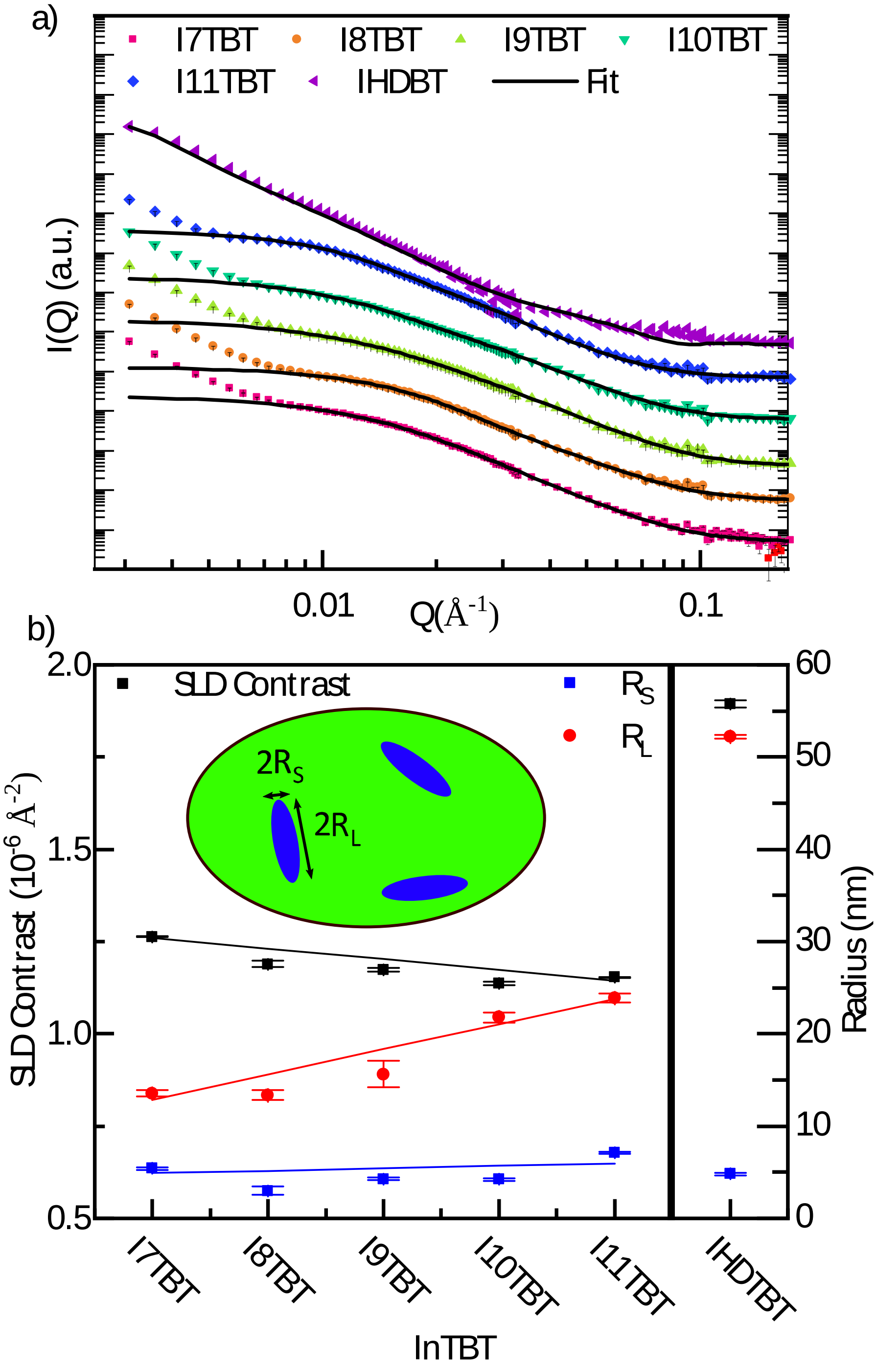

Figure 5: a) Small Angle Neutron Scattering data (offset for clarity) of InTBT:PCBM films. InTBTs with linear side chain were fit to an ellipsoidal form factor. IHDTBT was fit with a fuzzy sphere form factor at low Q and a spherical form factor at high Q, the combined fit is plotted. b)(Left axis) Scattering length density (SLD) contrast (black squares) between the form factor and surrounding matrix. (Right axis) Mean short (R_S)(blue squares) and long (R_L)(red dots) ellipsoidal radii from linear InTBT fits. For IHDTBT, the mean fuzzy sphere radii is plotted as (R_L), and the spherical radii is plotted as (R_S).

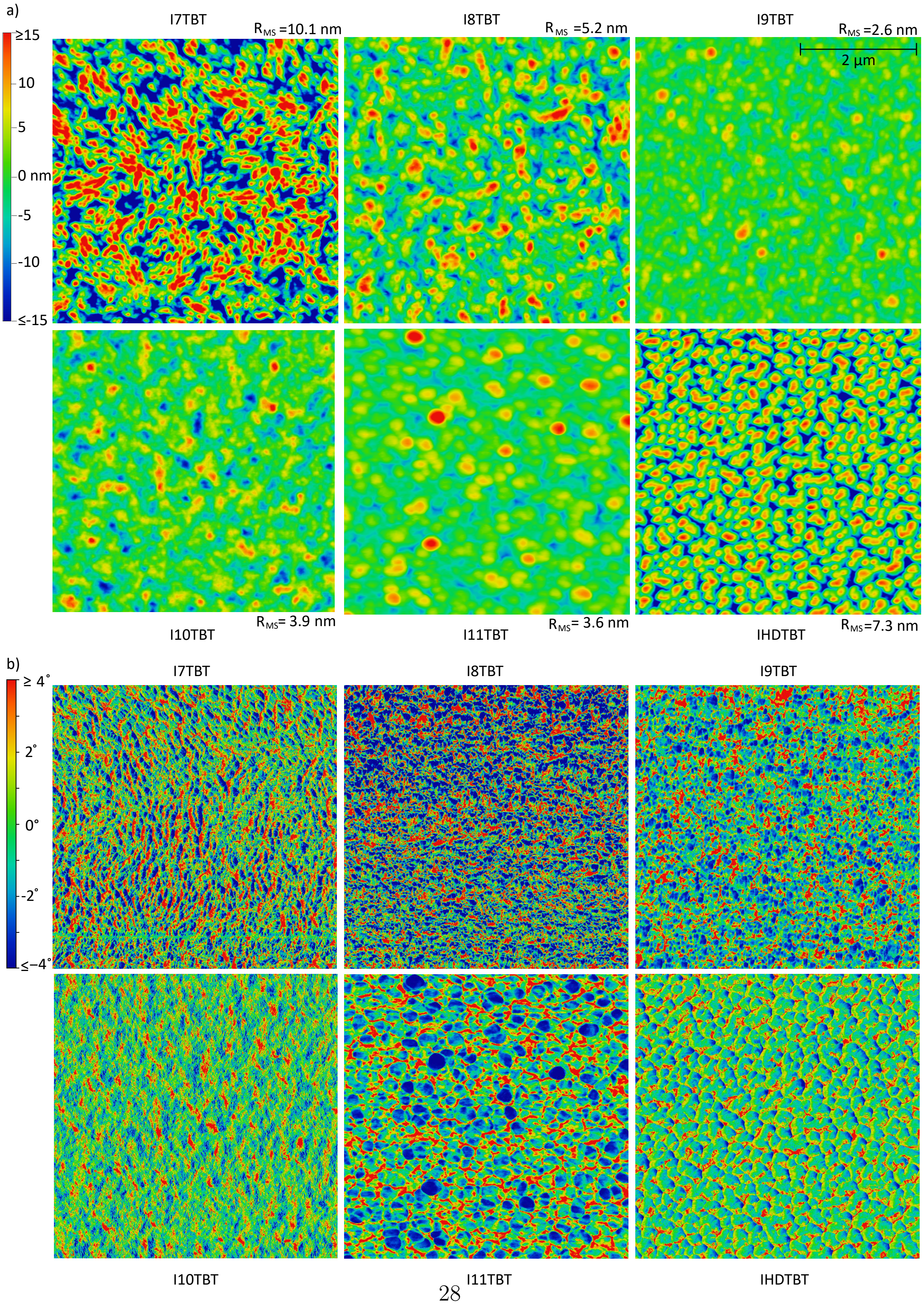

Figure 6: Atomic Force Microscope (a) height images with mean square roughness (R_{MS}) and (b) phase images of InTBT:PCBM films.

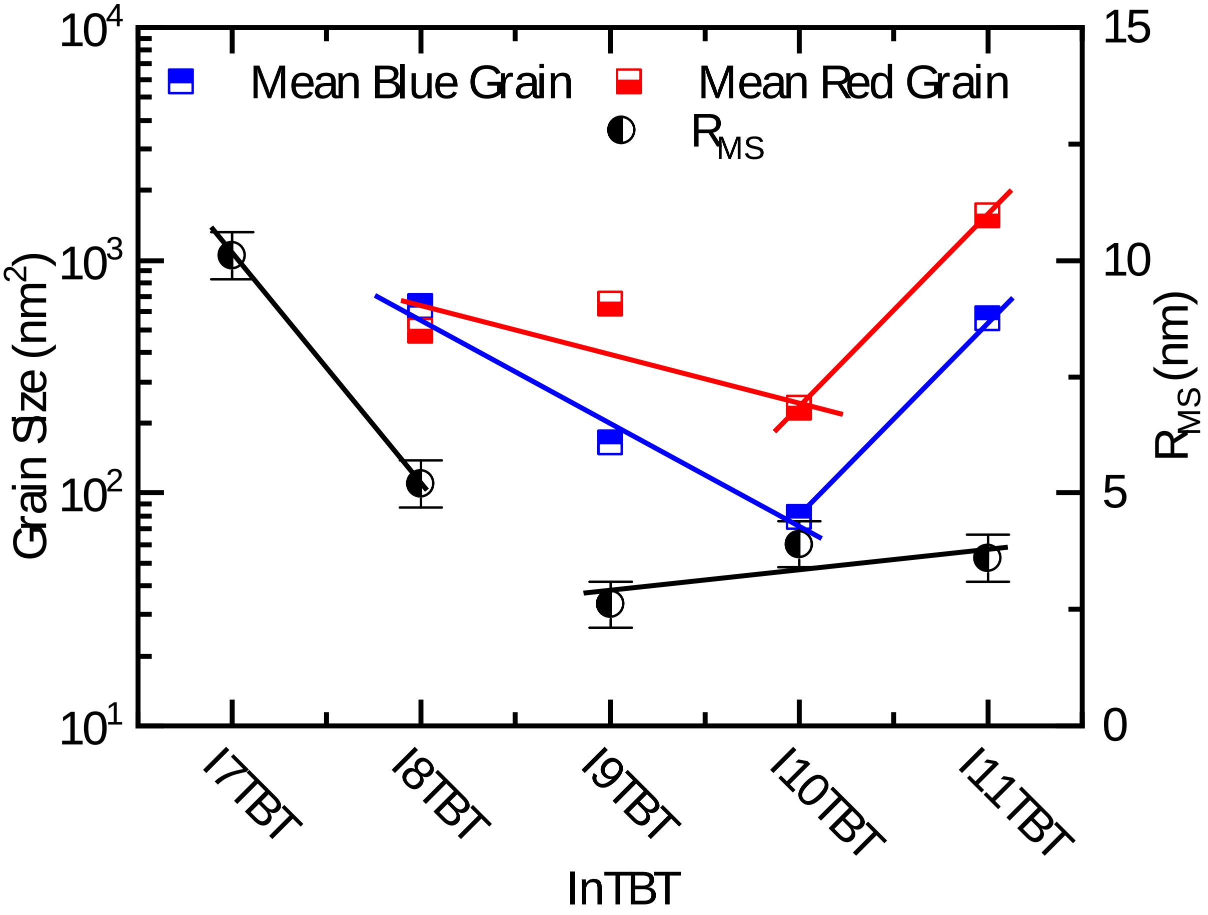

Figure 7: (Left) Mean grain size from AFM phase images of InTBT:PCBM films. Grains are defined by a cutoff phase shift; red (InTBT-rich) grains have greater than 4° phase shift and blue (PCBM-rich) grains have less than -4° phase shift. (Right) Root mean square roughness (R$_{MS}$) from corresponding AFM height images.

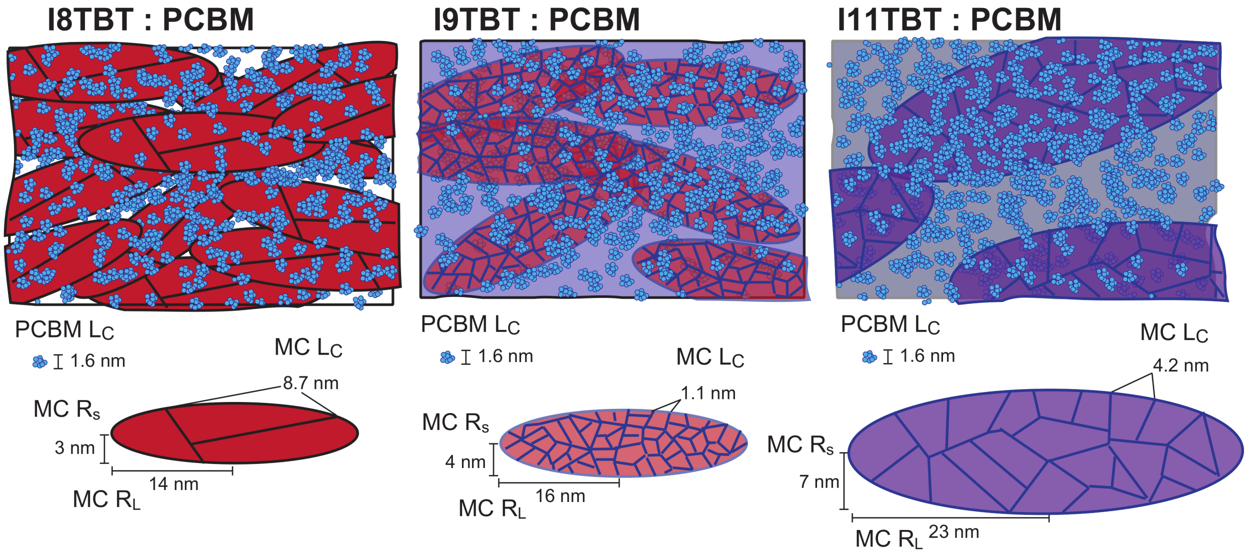

Figure 8: Illustration representing the bulk morphological differences observed between I8TBT:PCBM, I9TBT:PCBM, and I11TBT:PCBM films. L_C is coherence length from GIXRD, R_S and R_L are the short and long ellipsoidal radii from SANS.

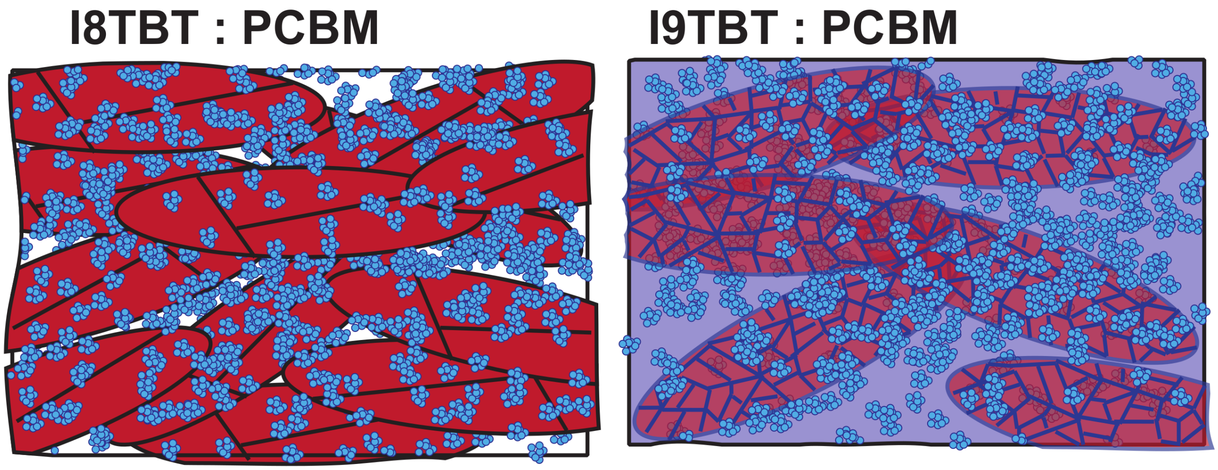

Figure 9: TOC Graphic